PAPER

Microwave synthesis of antimony oxide graphene nanoparticles – a new electrode material for supercapacitors†

Precious Ekwere, [ID] * Miranda Ndipingwi, Christopher Nolly, Chinwe Ikpo and Emmanuel Iwuoha [ID] *

For the first time, antimony oxide nanoparticles were produced using a microwave technique and evaluated as a supercapacitor electrode. The specific capacitance derived from the material's galvanostatic charge–discharge curve was 98 F g^{-1} in 1 M Li_2SO_4 electrolyte at 0.1 A g^{-1} current density. The charge storage mechanism visible in the CV curve is nearly rectangular and identical to the EDLC charge storage mechanism. Additionally, antimony species were chemically attached to graphene oxide using an antimony(III) chloride precursor and subsequently microwave aided procedures were used to convert the antimony species to SbO-G nanocomposites. The results of energy-dispersive X-ray spectroscopy demonstrated the pure character of the produced material. In a three-electrode cell arrangement, the resulting composite was electrochemically characterized. The cyclic voltammogram results showed that among the pristine SbO, graphene, and SbO-G materials, SbO-G had a higher specific capacitance value of 37.58 F g^{-1}, at a scan rate of 10 mV s^{-1}. The material has also demonstrated good conductivity characteristics based on electrochemical impedance spectroscopy research. After 3500 galvanostatic charge–discharge cycles, the material had excellent cycling stability of ~100%. All the remarkable capacitive properties demonstrated by this material indicate that it can be a viable choice in the field of energy storage devices.

1. Introduction

As a result of the rapid development in the chemical industry, finding a good balance between gaining more resources and maintaining a good sustainable environment is gaining more attention.[1] The need to have access to clean, reliable and renewable energy is an urgent need to create a sustainable society, therefore emerging technologies associated with energy conversion and storage have become highly paramount. A supercapacitor is one of the energy storage devices capable of satisfying our energy requirement. Compared to batteries, supercapacitors have a higher power density and life cycle and are safer to use.[2] Due to their high power density, their electrochemical and morphological characteristics have gained a great deal of interest in the manufacturing of these devices. Their energy density, however, is low, and new materials are always being researched to improve it.[3,4] Many antimony-based composites have recently demonstrated high capacity, which has spurred a lot of research into their use for energy storage.

Because of its large theoretical capacity and adequate working voltage, antimony chalcogenide, for example, is now widely researched as a promising electrode material for batteries. Currently, antimony is widely used in semiconductors, anti-friction alloys, small arms and tracer bullets, and cable sheathing, as a flame retardant addition in large amounts[5] and has a large alloying/dealloying potential as well as a high capacity (660 mA h g^{-1}).[6] It is well known that antimony corrodes easily, and can flow through a negative electrode in lead batteries, through corrosion of current leads, leading to a reduction in battery service life.[7] However, further research has shown that the antimony-containing corrosion layer discharges slowly, allowing the active material to discharge faster than the corrosion layer and preventing the formation of a passivation layer at the electrolyte/active material interface.[8] As a result, it appears that adding antimony to the electrode's active material effectively reduces capacitance loss. Antimony has been widely investigated as an addition in newer energy storage sources, such as lithium-ion batteries (LIBs), liquid metal batteries, and fuel cells. Antimony is hypothesized to perform two roles in LIBs: first, it functions as a spacer to prevent major volume changes in the electrode during the charging/discharging cycles; second, it can hold up to three lithium atoms and provide additional capacitance. Metallic antimony in a sodium-ion battery (SIB) or LIB, on the other

SensorLab (University of the Western Cape Sensor Laboratories), Chemical Sciences Building, University of the Western Cape, Bellville 7535, Cape Town, South Africa. E-mail: 3822315@myuwc.ac.za; eiwuoha@uwc.ac.za

† Electronic supplementary information (ESI) available. See DOI: https://doi.org/10.1039/d3na00514c

hand, exhibits a considerable volume expansion during sodation/desodation or lithiation/delithiation in each battery system, resulting in a decrease in the device's long-term cycle performance. Several methods have been employed to decrease volume expansion, including (1) the production of metallic alloys, (2) the formation of a stable heterostructure oxide (*e.g.*, Sb/S_2bO_3), and (3) nanoscale tailoring and anchoring in a carbon matrix. Antimony's excellent performance and long and steady cycle life can be achieved by anchoring it in or with carbon. Several studies on the synthesis of an antimony carbon composite for usage in energy storage have recently been published.

Ciszewski *et al.*[9] reported on reduced graphene oxide for high-performance supercapacitor electrodes using an established polyol method. Sahoo *et al.*[10] designed sulfur-doped carbon sheet anchored or encapsulated Sb_2S_3 nanoparticles for high-performance using microwave-assisted synthesis. Xio *et al.*[11] presented a novel tin antimony oxide/graphene anode material for lithium-ion batteries, by a hydrothermal method. Hai *et al.*[12] also synthesized a paste electrode made of multiwall carbon nanotubes modified with antimony oxide (Sb_2O_3/ MWCNTs) for simultaneous electrochemical detection of cadmium and lead ions. The key goals of combining carbon with Sb as the buffer layer are to (i) provide structural stability with improved conductivity and surface area, hence increasing the capacitance, and (ii) decrease the volume expansion and agglomeration of Sb particles during the cycle life. LIBs, as well as catalytic and supercapacitive applications, have shown that Sb particles anchored in carbon and Sb-based chalcogenides offer greater potential.

In this study we present the synthesis of two types of materials, SbO and SbO-G nanoparticles, using a simple microwave approach. Various techniques are used to analyze the structure, morphology, crystalline phase, and surface area of both samples. In a 1 M Li_2SO_4 electrolyte, the SC performance of each material is measured using a three-electrode electrochemical setup. In a positive potential window (0–0.6 V), the SbO and SbO-G electrodes exhibit an electrostatic double-layer capacitance characteristic. The specific capacitance, rate capability, energy density, power density, and durability of an asymmetric SC were also tested. The carbon in the SbO nanoparticles served as a buffer layer that prevented structural degradation while also increasing the effective contact area between the electrode and the electrolyte. These studies suggest that antimony chemistry could be important in the development of new energy storage devices. Although antimony has been used severally as a dopant or an additive in supercapacitor materials, as far as we know, we have not found any application of antimony oxide as a supercapacitor electrode reported. This research could lead to new ideas for using SbO-based electrodes with high reversible capacities in SC applications.

2. Experimental

2.1 Materials

Microcrystalline graphite (2–15 μm, 99.99%) was purchased from Alfa Aesar (Kandel, Germany). Nickel foam (1.6 mm thick, 0.25 μm pore diameter) was purchased from MTI Corporation (Richmond, California, USA). Hydrogen peroxide solution (30 wt% in water, American Chemical Society (ACS) reagent), concentrated hydrochloric acid (reagent grade and assay 36.5– 38.0%), sodium borohydride (98.0%), potassium permanganate (≥99.0%, ACS reagent), concentrated sulphuric acid (99.999%), antimony pentachloride (99.999% trace metal bases), poly-tetrafluoroethylene (mean particle size 20 μm), activated charcoal (Norit® pellets), anhydrous *N*-methyl-2-pyrrolidone (99.5%) and carbon black (4 μm mesoporous carbon matrix, ≥99.95% metal bases), ethylene glycol (EG) (99.8%), and ethanol (absolute, ≥99.8%) were purchased from Sigma-Aldrich (St Louis, Missouri, USA) and were all used without further purification.

2.2 Microwave-assisted synthesis of SbO and SbO-G nanocomposite

The MW-assisted synthesis of SbO was carried out using an Anton Parr multi-wave Pro microwave system. It is equipped with an IR temperature sensor that controls the temperature during the process. $SbCl_5$ (1 mmol) was added to 30 mL of ethylene glycol with continuous stirring for 0.5 h. $NaBH_4$ (1.5 g) was slowly added to the above-mixed solution, sonicated for 10 min, and allowed to cool. The resultant mixture was MW-irradiated at 190 °C for 10 min. The resulting products were separated by centrifugation, washed with deionized water, and dried at 60 °C under vacuum for 12 h.

In another reaction vessel, one hundred milligrams of synthesized GO are added to 30 mL of ethylene glycol and sonicated for 2 h to form a homogeneous dispersion. $SbCl_5$ (1 mmol) was added to the dispersed solution and sonicated for 0.5 h. $NaBH_4$ (2 g) was slowly added to the above mixture, which was sonicated for 10 min and transferred to a microwave vessel. The resultant mixture was MW-irradiated at 190 °C for 10 min. The resulting products were separated by centrifugation, washed with deionized water, and dried at 60 °C under vacuum for 12 h.

2.3 Material characterization

The elemental and morphological composition of the nanoparticles were obtained using a Carl ZEISS ULTRA scanning electron microscope GmbH, fitted with an energy dispersion spectrometer (Jena, Germany). All analysis was performed on a nickel–copper grid. The samples for TEM characterization were drop-coated into the Cu TEM grids and scanned in a high-resolution transmission electron microscope (HR-TEM) with an FEI Tecnai G20 F20X-Twin MAT 200 kV Field Emission Transmission Electron Microscope (Eindhoven, Netherlands) equipped with both EDS and selected area electron diffraction (SAED). The X-ray powder diffraction (XRD) pattern was obtained for all the nanoparticles with a D8 advance multipurpose X-ray diffractometer (BRUCKER-AXS, Berlin, Germany) using copper kα1 radiation (λ ∼ 0.154 nm) operating at 40 kV and 40 mA. The functional group present in the sample was determined using a PerkinElmer Spectrum 100 series Attenuated Total Reflectance (ATR) Fourier Transform Infra-red

spectrometer with 4 cm^{-1} resolutions (PerkinElmer, Boston, MA, USA). The particle size distribution was determined by a small-angle X-ray scattering (SAXS) measurement, performed on an Anton Paar GmbH SAXSpace P/N 100100 (Graz, Austria). It was equipped with a 1 D Mython 2 position-sensitive detector with a beamstop alignment; a copper Kα (0.154 nm) instrument radiation was used. The nanoparticle Raman spectra were obtained using an Xplora Olympus BX41 Raman Spectrometer (Horiba, Tokyo, Japan) using a 532 nm laser as the excitation source. Optical absorption spectra were acquired from ethanolic dispersions of the nanocrystals at room temperature using a Varian Cary 300 UV-Vis-NIR spectrophotometer (Agilent, Santa Clara, CA, USA). At room temperature, infrared spectroscopic investigations between 4000 and 400 cm^{-1} were carried out. The powdered nanocrystals were deposited on a diamond disc, and infrared spectra were acquired using an Attenuated Total Reflectance/PerkinElmer Spectrum 100 Series Fourier Transform Infrared (FTIR) Spectrometer (PerkinElmer, Boston, MA, USA). The photoluminescence properties were studied with a NanoLog HORIBA using the software FluorEssence V3.9
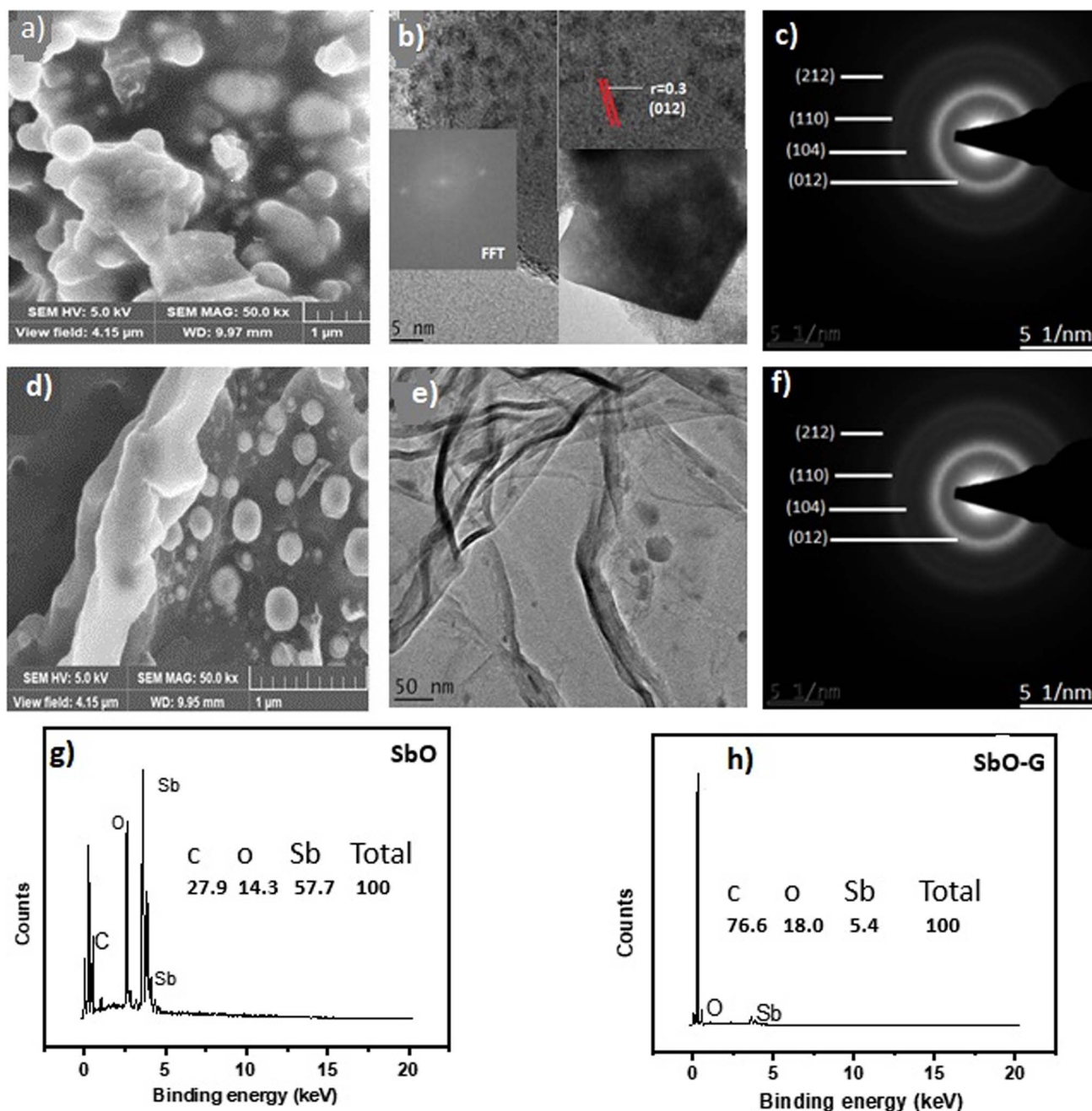

Fig. 1 SbO: (a) SEM image, (b) TEM image showing the lattice fringes (the inset is the FFT), (c) SAED pattern, (g) EDS spectrum (the inset is the percentage elemental composition) and SbO-G: (d) SEM image, (e) TEM image showing the graphene sheet (f) SAED pattern, (h) EDS spectrum (the inset is the percentage elemental composition).

(Johannesburg, South Africa). All electrochemical studies were performed on a VMP-300 potentiostat from Bio-Logic Instruments (France).

2.4 Electrode preparation and electrochemical measurements

To prepare the working electrode, the active material, SbO and SbO-G (70%), a conducting agent, carbon black (20%) and a binder, polytetrafluoroethylene (10%) were mixed in a mortar, and crushed to a fine powder, then 3 drops of anhydrous *N*-methyl-2-pyrrolidone were added and mixed to form a uniform slurry. Nickel foam was cut into rectangular shapes of 0.5×1 cm^2 and coined shapes of 20 mm in diameter. The foams were cleaned to remove all surface oxide layers in 1 M HCl solution, absolute ethanol and deionized water, respectively, with ultrasonication for 15 min in each solvent, and dried at 90 °C for 12 h. The homogeneous paste was coated on 0.5 cm^2 diameter of the nickel foam and dried at 80 °C for 12 h. In a three-electrode cell setup, Ag/AgCl and Pt wire were used as the reference and counter electrode respectively, while for the full cell, the paste was coated onto the coin-shaped nickel foam and assembled in a Swagelok with activated carbon as the negative electrode. The cyclic voltammograms were recorded between −0 and 0.6 V potential window at different scan rates; the electrochemical impedance measurements were obtained at a frequency range of 0.1 MHz to 100 MHz with 10 points per decade, and the galvanostatic charge–discharge profiles were measured at different current densities. All electrochemical characterization of materials was done in the three-electrode cell using 1 M Li$_2$SO$_4$ electrolyte. The device testing was done at 1.8 V in the same electrolyte.

3. Results and discussion

3.1 Morphological studies

3.1.1 Scanning electron microscopy (SEM). The surface morphology, mean particle size, and shape of SbO and SbO-G nanoparticles were studied using SEM. Fig. 1a depicts spherically shaped particles ranging in size from 10 to 50 nm that are uniformly dispersed. The SEM microgram of SbO-G shows a visible graphene sheet with SbO nanoparticles dispersed randomly on the surface. As a result, antimony nanoparticles must have acted as spacers, reducing graphene aggregation. This will result in increased surface area and, consequently, increased charge storage and capacitance.

3.1.2 Transmission electron microscopy (TEM). For the pure SbO, the TEM image in Fig. 1b shows highly spherically shaped randomly distributed nanoparticles as seen in the SEM with particle sizes ranging from 10 to 45 nm. The spherical nanoparticles may be seen randomly distributed on the surface of the graphinized material with an average particle size between 10 and 40 nm. This shows that SbO nanoparticles were successfully graphinised. Despite the high degree of aggregation, the material's small grain size indicates that it is highly permeable.[13,14] Porosity would improve the ion transfer process and, as a result, the energy storage efficiency.[15] In the

corresponding SAED pattern, all rings can be indexed to the diffraction peaks of orthorhombic Sb$_2$O$_3$. Due to the crystallinity of the material, the selected area electron diffraction (SAED) pattern exhibits concentric circles, indicating that the material is crystalline in the (212), (110), (104), (012) directions for SbO and (012), (104) and (110) directions for SbO-G. Higher the crystallinity of the material, faster the ion transit within the grains and higher the conductivity.[14] The interlayer spacing was also calculated from the SAED images. The *d* spacing for SbO and SbO-G was calculated to be 2.07 and 2.32 nm respectively. This shows that the incorporation of graphene into the SbO lattice increased the interlayer spacing of the material. The increased spacing will give rise to quicker ion movement thus higher power density. The HRTEM confirms a structural change with the inclusion of graphene.

3.2 Spectroscopic studies

3.2.1 Energy-dispersive X-ray spectroscopy (EDS). The synthesis of SbO and SbO-G nanoparticles has been verified using EDS. Fig. 1g and h show EDS focused on several spectral areas and accompanying peaks. The presence of Sb and O in SbO is confirmed by EDS analysis. In SbO-G, Sb, O, and C elements are present. In the inset, the quantity of each element measured in atom per cent is displayed. The result shows that the composite has a considerable quantity of graphene, which will improve the composite's stability and limit any volume expansion caused by antimony.

3.2.2 X-ray powder diffraction (XRD). The crystal structure of SbO-G was investigated using XRD analysis. The XRD spectra of SbO and SbO-G are shown in Fig. 2a. SbO and SbO-G were indexed into an orthorhombic structure. Space group (*Pnnm* (58); JCPD card no. 2_34-0340), with lattice parameter $a = 5.95140$ Å and $c = 6.67430$ Å. The sample shows diffraction peaks at $2\theta = 28.59°$, $39.98°$, $41.84°$ $51.52°$, $68.52°$, $65.88°$ and $75.26°$ which belong to the (012), (104), (110), (015), (212), (024), (116), (122) and (214) phases of SbO$_2$ for both SbO and SbO-G samples. Both samples seem to have the same phases, however, with the addition of graphene, the peak intensity increased and broadened in SbO-G. For example, when comparing the intensities of SbO and SbO-G XRD diffraction peaks, the (012) plane in the XRD spectrum had the highest diffraction peak intensity. A graph of SbO overlayed on SbO-G as shown in the ESI† clearly shows the higher peak intensity of SbO-G compared to SbO. The (012) plane of SbO was situated at 28.59°, and the (002) plane of graphene was also located at 28.54°. The coincidence of the two crystal surface diffraction peaks may be the cause of the increase in the intensity of (012) diffraction peaks in the SbO-G XRD spectrum.[11] The crystal plane values of SbO-G (002) are $2\theta = 28.59$ and $d_{012} = 3.12$, respectively, compared to those of SbO-G, which are $2\theta = 28.4$ and $d_{012} = 3.29$. The interplanar spacing of SbO-G (3.29) is slightly higher than that of SbO (3.12) due to the retention of a few functional groups and curved surface structures following reduction.[16] The most intense peak in the SbO-G composite ($2\theta = 28.54°$) is slightly shifted to a lower angle as compared to pristine SbO nanoparticles ($2\theta = 28.59°$) indicating the
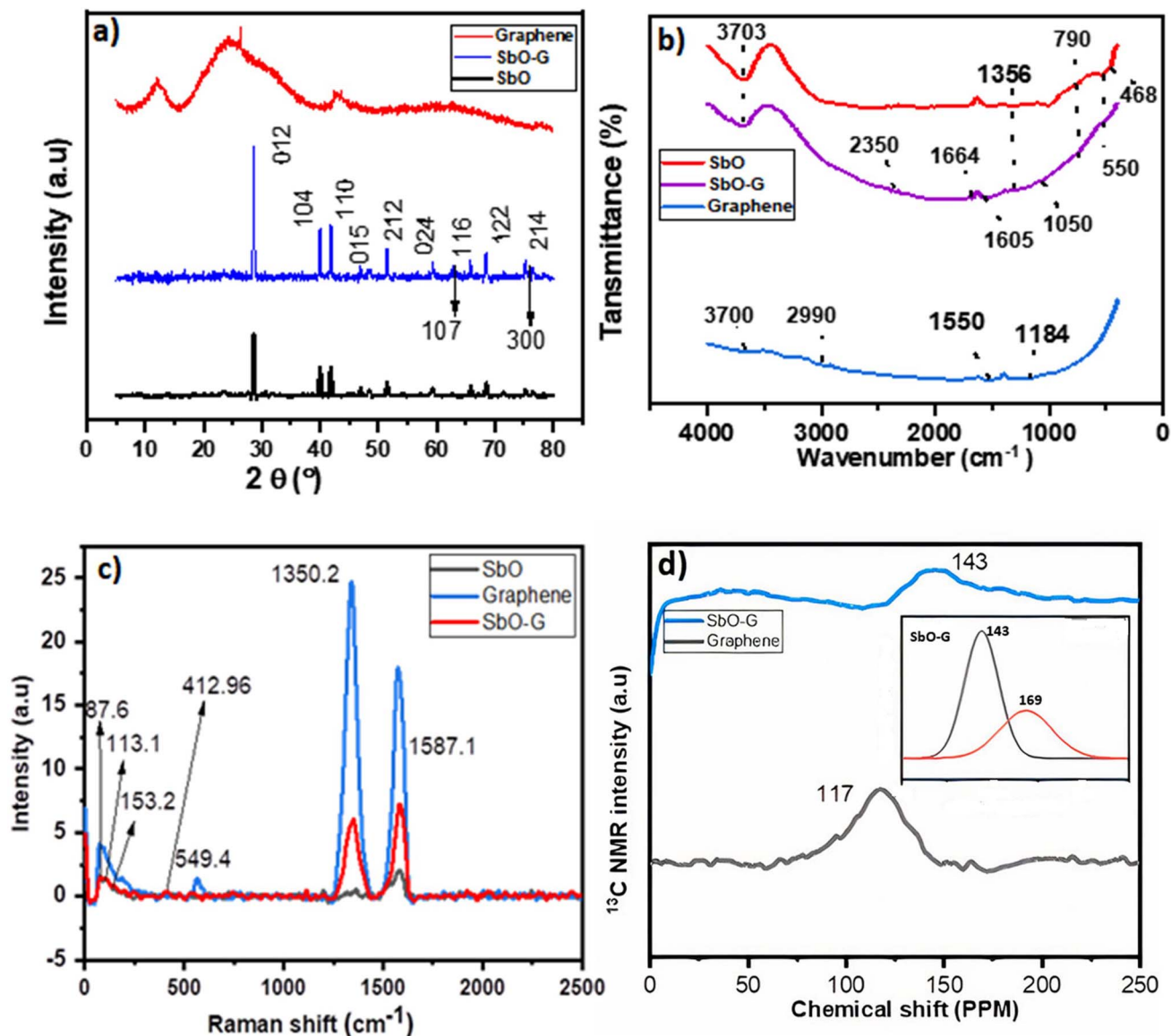
Fig. 2 SbO and SbO-G overlayed on graphene (a) XRD analysis showing the change of intensity and peak position of the crystal phases; (b) FTIR spectra, (c) Raman spectra, (d) NMR spectra of graphene and SbO-G (the inset is the deconvoluted 126 ppm peak of SbO-G).

enlargement in SbO interlayers due to defects/embedding of the graphene nanoparticles.[14] A clear shift in the interlayer spacing between SbO and SbO-G indicates that the addition of graphene can effectively expand the interlayer spacing of the composite, which will facilitate the diffusion and transport of electrolyte ions during the charge/discharge process.[17,18]

Crystal size was also estimated using the Debye–Scherrer formula for the most intense peaks in the XRD patterns. The size was an average of ~46.63 nm and ~40.3 nm for SbO and SbO-G respectively confirming the smaller crystal size in SbO-G as estimated by the SEM and TEM analysis.

3.2.3 Fourier transform infra-red spectroscopy (FTIR). The FTIR absorption spectra of SbO and SbO-G in the 4000–400 cm^{-1} region are shown in Fig. 2b. The investigation was carried out to determine the presence of bending or stretching vibrations in the synthesized SbO and SbO-G. The distinctive

OH stretch is confirmed by the broadband at 3669 cm^{-1} in the SbO spectrum. The vibration of molecular water's hydroxyl groups and the stretching vibration of the peroxo group induce the absorption band around 1647 and 1067 cm^{-1}. The Sb–O

Table 1 Functional groups and vibrational bands of SbO and SbO-G

Functional group	Material/wavenumber (cm^1)	
	SbO	SbO-G
O–H	3669	3703
C–H		2350
C=O		1664
–O–O–	1067	
C–O		1050
Sb–O	550	512

stretching is visible in the SbO spectrum at 468, 550 and 790 cm^{-1}.[19] In the FTIR absorption spectrum of SbO-G, distinctive OH stretch is confirmed by the vibrational band at

3790 cm^{-1} and broadband at 3385 cm^{-1} in the spectrum. The bending and stretching of C–H, C=C=C, C–O, and C–C groups induce the absorption band around 3000–1000 cm^{-1}. The
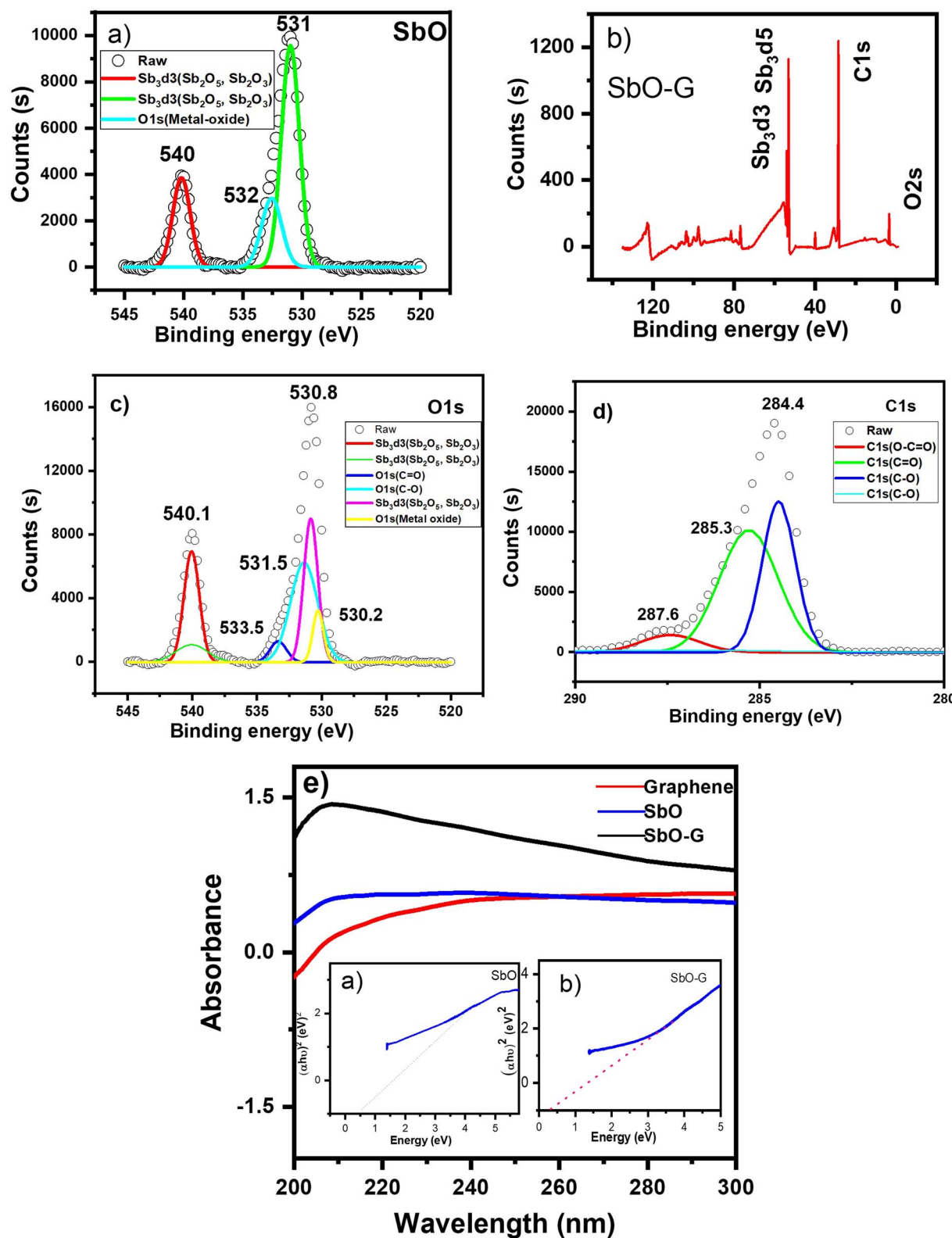

Fig. 3 XPS spectra of; (a) SbO; Sb 3d + O1s, (b) SbO-G; (c) Sb 3d + O1s, (d) C1s scan (e), the UV-vis spectra of SbO and SbO-G overlayed on graphene and the inset (a and b) is their corresponding Tauc plots.

vibrational band at 512 cm^{-1} is characterized by the presence of SbO, whereas the tiny band at 776 cm^{-1} is induced by the asymmetric stretch of SbO. The shift in the band position and intensity for SbO-G in comparison to the pristine materials plus the presence of the bending and stretching of the graphitic bonds in the SbO-G spectrum indicate the creation of a new structural material. All distinct functional groups present in the samples are shown in Table 1.

3.2.4 Raman spectroscopy. The SbO and SbO-G materials were further characterized using Raman spectroscopy, which provided the structural fingerprint by which antimony oxide is detected. SbO and SbO-G revealed a visible peak at 87.6 cm^{-1} that belonged to F_{2g} Sb_2O_3 in the Raman spectra, Fig. 2c.[20] The typical E_g (113.1 cm^{-1}) and A_{1g} (153.2 cm^{-1}) belonging to the in-plane and out-of-plane vibrational modes of Sb–O were also identified,[21–23] confirming that SbO nanoparticles have been obtained after reduction. Additional peaks related to antimony oxides (Sb_2O_4) were detected at 412.96 and 549.47 cm^{-1}, confirming the production of microcrystalline Sb_2O_4.[24] The Raman spectra of SbO-G were not different from those of pure SbO, but the typical peaks of carbon D (2) and G (5) bands were present, showing that the *in situ* reductions of SbO and GO to SbO-G were successful using microwave radiation.[25] The G band appears in SbO because of the carbon glue used to adhere the samples to the SEM stubs. The graphene in SbO-G has less defects than pristine graphene, based on the I_D/I_G ratio and the very low intensity of D.[26] This is obvious in the TEM results.

3.2.5 Solid-state nuclear magnetic resonance spectroscopy (NMR). Fig. 2d shows the NMR spectra of SbO-G and graphene. The carbon environment of pure graphene was compared to that of graphene samples with SbO-G. The prominent peak at 117 ppm, which belongs to graphitic sp^2 carbon as seen in graphene, shifted to 143 ppm, while a shoulder peak can be seen at 169 ppm which when deconvoluted (the inset) reveals a broad peak with FWHM-34 ppm, indicating that the chemical environment of carbon must have been influenced by the interaction of SbO nanoparticles with graphene.[27]

3.2.6 X-ray photoelectron spectroscopy. XPS is a useful supplementary technique for determining the oxidation states and stoichiometry of SbO and SbO-G. In Fig. 3a, the elements Sb and O were detected in the SbO nanomaterial. The high-resolution O1s spectrum of SbO was split into three peaks at 540, 532 and 531 eV. The peaks at 540 and 531 eV can be attributed to Sb_2O_5/Sb_2O_3, implying that the SbO sample contains a considerable quantity of Sb_2.[28] The MW synthesis successfully introduced antimony atoms into the graphene matrix, according to Fig. 3b. The high-resolution Sb 3d + O1s spectrum of SbO-G (Fig. 3c) was split into six peaks at 540, 533, 531, and 530 eV. The peaks at 540 and 530 eV can be attributed to Sb_2O_5/Sb_2O_3, implying that the SbO-G samples contain Sb_2 in a large amount at its outer surface. C=O and C–O can be ascribed to the 533 and 531 eV peaks, respectively. The presence of Sb_2O_5 is suggested by the high peaks at 540 and 530 eV. The presence of carbon–oxygen components, such as C–O, C=O, and O–C=O, was demonstrated by the presence of peaks at 287, 285, and 284 eV in the C1s spectrum (Fig. 3d). When Sb3 d3 of SbO-G is compared to SbO (ESI† Fig. 11), a change to lower

binding energy is seen, implying a larger electron density at Sb3 sites in the SbO-G sample.[29,30]

3.2.7 UV-vis spectroscopy. Fig. 3e shows the UV-vis absorption spectra of SbO and SbO-G. The UV-vis absorption spectra revealed that SbO and SbO-G have a broad UV-vis absorption range, with the highest absorption at 206 nm. The absorption intensity of SbO-G is higher than that of pure SbO, which may be attributed to the sum of the absorption for graphene and SbO,[31,32] indicating that the SbO-G nanoparticles were successfully synthesized. With the addition of graphene, the curve exhibits a more evident exponential decay, indicating that the SbO-G nanoparticles have increased dispersion capacities. Using the Tauc plot from Origin software (the inset a and b), the band gaps of SbO and SbO-G were estimated to be 0.46 and 0.34 eV, respectively.[31] When compared to pure SbO nanoparticles, the bandgap of the SbO-G composite is lowered due to the development of Sb–O–C bonds.[32,33] The charge transmission is facilitated by the link that exists between Sb and C. It is worth mentioning that the lower bandgap value found in this study could be attributed to the enhanced crystallinity of the nanoparticles.[34]

3.3 Electrochemical studies

3.3.1 Cyclic voltammetry. Cyclic voltammetry was used to investigate the SbO and SbO-G compounds in a 1 M Li_2SO_4 electrolyte. At scan rates ranging from 10 to 100 mV s^{-1}, capacitive currents were observed between 0.0 and 0.6 V vs. Ag/AgCl electrode. Both materials showed a steady increase in cathodic currents as potential rises with no pseudocapacitive/redox peak (Fig. 4a and b). This demonstrates superior capacitive behaviour, resulting in increased power.[33] As the scan rate increases, the capacitive currents in the cyclic voltammograms indicate a substantial increase. This means the charge storage mechanism is capacitive and the process is reversible electrochemically.[34] Voltammograms of SbO have a nearly rectangular shape, resembling the behaviour of a perfect EDLC. According to Trasitti et al.,[35] the charge storage mechanism of a metal oxide is divided into outer and inner site charge contributions.[36] As a result, at a high scan rate, when the inner sites are all exonerated from the capacitance contribution, the charge/discharge occurs so quickly at the outer site, giving rise to the rectangular shape seen in the carbon voltammogram. Secondly, if the material is porous and the inner sites are easily accessible, charge and discharge will occur at a rapid rate, resulting in a rectangular shape.[37] Therefore, the voltammogram of SbO suggests high porosity of the material. SbO-G voltammogram shows a slight deviation from perfect EDLC behaviour. The quasi-rectangular voltammogram of the SbO-G materials demonstrates that EDLC and the pseudocapacitance charge storage mechanism both play a role. The deviation of the voltammogram from the ideal rectangular form increased as the voltage scan rate increased. This could be due to the electrode's electrochemical polarization. The pseudocapacitance contribution and the electrochemical polarization of the electrode are caused by the numerous functional groups present in the SbO-G as shown in the FTIR.[38] The specific capacitance of the three materials was calculated from the equation below:
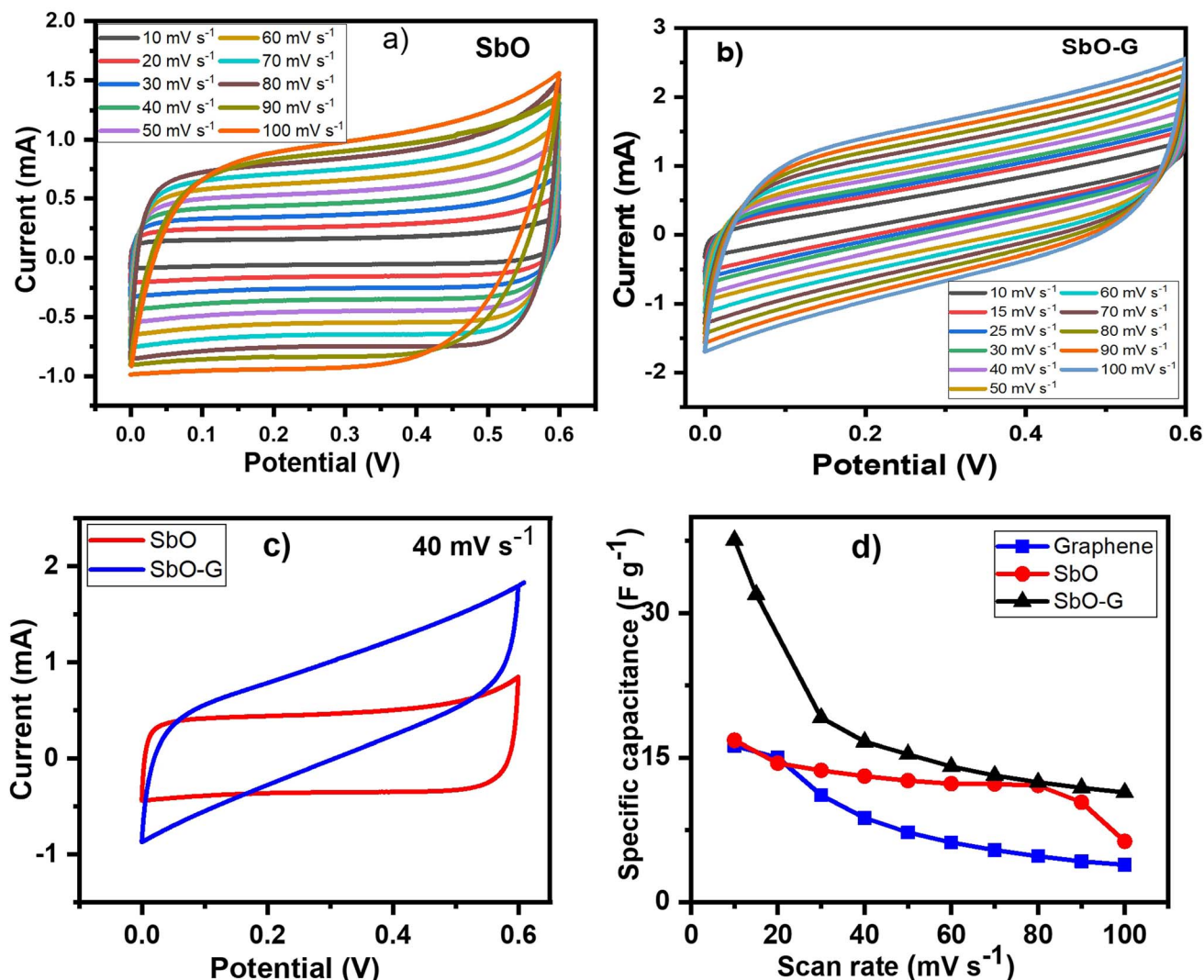
Fig. 4 SbO and SbO-G: (a and b) CV plots at different scan rates, (c) CV plots comparing their voltammograms at 40 mV s^{-1} scan rate, (d) their specific capacitances at different scan rates. All analysis was done in 1 M Li$_2$SO$_4$ electrolyte.

$$C_{sp} = \frac{1}{2mv \triangle V} \int_{-v}^{+v} I dv \tag{1}$$

where m is the active mass of the electrode (g), v is the scan rate (V s^{-1}), ΔV is the potential window in V and $\int_{-v}^{+v} I dv$ is the charge obtained from the integrated area of the voltammogram. SbO-G showed a better electrochemical performance with a specific capacitance of 37.58 F g^{-1} at 10 mV s^{-1} and up to 11.41 F g^{-1} at 100 mV s^{-1}. The values were 16.80 F g^{-1} at 10 mV s^{-1} and 6.32 F g^{-1} at 100 mV s^{-1} for SbO. The CV curves of SbO and SbO-G are shown in Fig. 4c at a scan rate of 40 mV s^{-1}. The area under the CV curve of SbO-G is greater than the area of SbO. Because the average value of the area under the CV curves is directly related to the capacitance value, this finding demonstrated that SbO-G had enhanced capacitive behavior. Greater the area under the CV curves, greater the amount of charge held by the electrode material. The high capacitance of SbO-G is mostly owing to the composite's large specific surface area and the high conductivity of graphene.[39]

The specific capacitance values are plotted against potential sweep rates as shown in Fig. 4d. The specific capacitance values for both materials gradually reduced when the voltage scan rate was increased as shown in Table 2. This is owing to the short time interval, which precludes the contribution of the electrode's inner surfaces.[40]

3.3.2 Galvanostatic charge discharge. The performance of SbO and SbO-G electrodes was investigated at current densities of 0.1, 0.2, 0.4, 0.5, 0.6, 0.8, 1, 2 and 5 A g^{-1} (Fig. 5a and b). The SbO-G electrode's GCD curves show a high specific capacitance when compared to SbO. The presence of typical triangular curves confirms the electric double layer capacitive charge storage mechanism occurring at the electrode-electrolyte interface.[41] The GCD curves are nearly symmetrical, with only a minor voltage drop due to the equivalent series resistance (ESR). The timing for the charge and discharge process is similar especially at higher current, indicating a high coulombic efficiency and electrochemical reversibility.[39] These observations are consistent with the oxidation and reduction

Table 2   The capacitance of SbO and SbO-G at different scan rates

Scan rates (mV s^{-1})	Capacitance (F g^{-1})	
	SbO	SbO-G
10	16.80	37.58
30	13.69	19.14
40	13.10	16.65
50	12.63	15.37
60	12.32	14.10
70	12.28	13.17
80	12.13	12.46
90	10.38	11.88
100	6.32	11.41

profiles reported in the CV curves. The specific capacitance was determined using the equation

$$C_s = \frac{I \times t}{m \times V - IR_{drop}} \quad (2)$$

where I is the constant current, m is the active material mass, and t is the discharge time corresponding to the voltage change, V.[22] Fig. 5d shows a comparison of the rate capabilities of SbO and SbO-G electrodes at various current densities. At a current density of 5 A g^{-1}, SbO-G has a specific capacitance 3.27 F g^{-1}, which is substantially lower than that of SbO (11.3 F g^{-1}). From the rate capability analysis, the SbO electrode exhibits better capacitance retention retaining ~80% of its capacitance at 1 A g^{-1} and ~40% at 5 A g^{-1}. The SbO-G electrode has the highest specific capacitance at the same current density when compared to SbO electrodes. The highest capacitance of the SbO-G electrode, for example, reached 98 F g^{-1} at 0.1 A g^{-1}, while that of SbO was 25.11 F g^{-1}. This is due to the contribution of EDLC and pseudocapacitance and the more porous microstructure, which facilitate electrolyte infiltration and contribute to the development of electrical double-layer capacitance. The specific capacitance decreases as the current increases (5d). The drop in specific capacitance values was noticeable in the discharge time of GCD curves. This drop-in
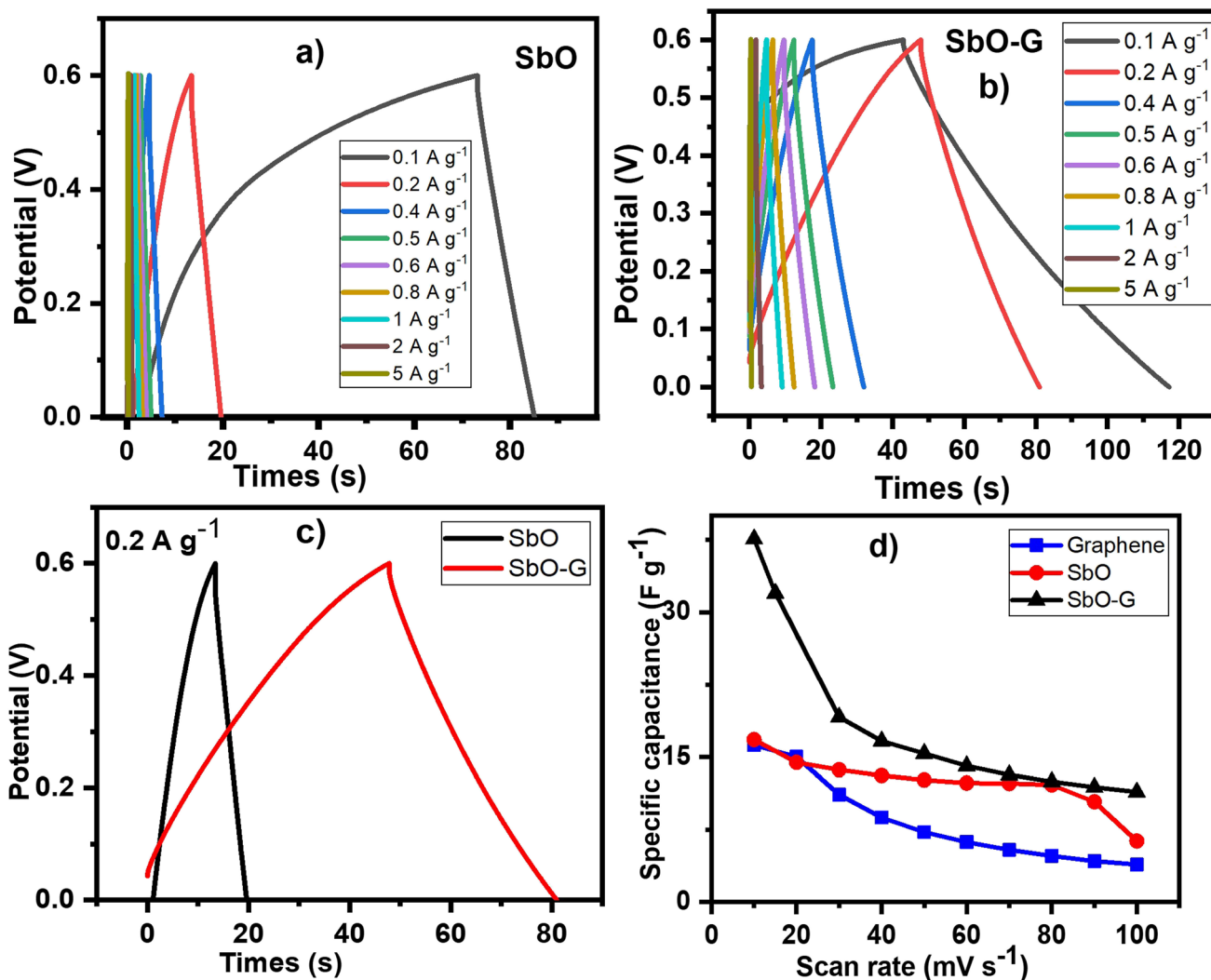

Fig. 5   SbO and SbO-G: (a and b) GCD plots at different current densities, (c) GCD plots comparing their charge and discharge profile at 0.2 A g^{-1} current density, (d) is their specific capacitance at different current densities. All analysis was done in 1 M Li$_2$SO$_4$ electrolyte.
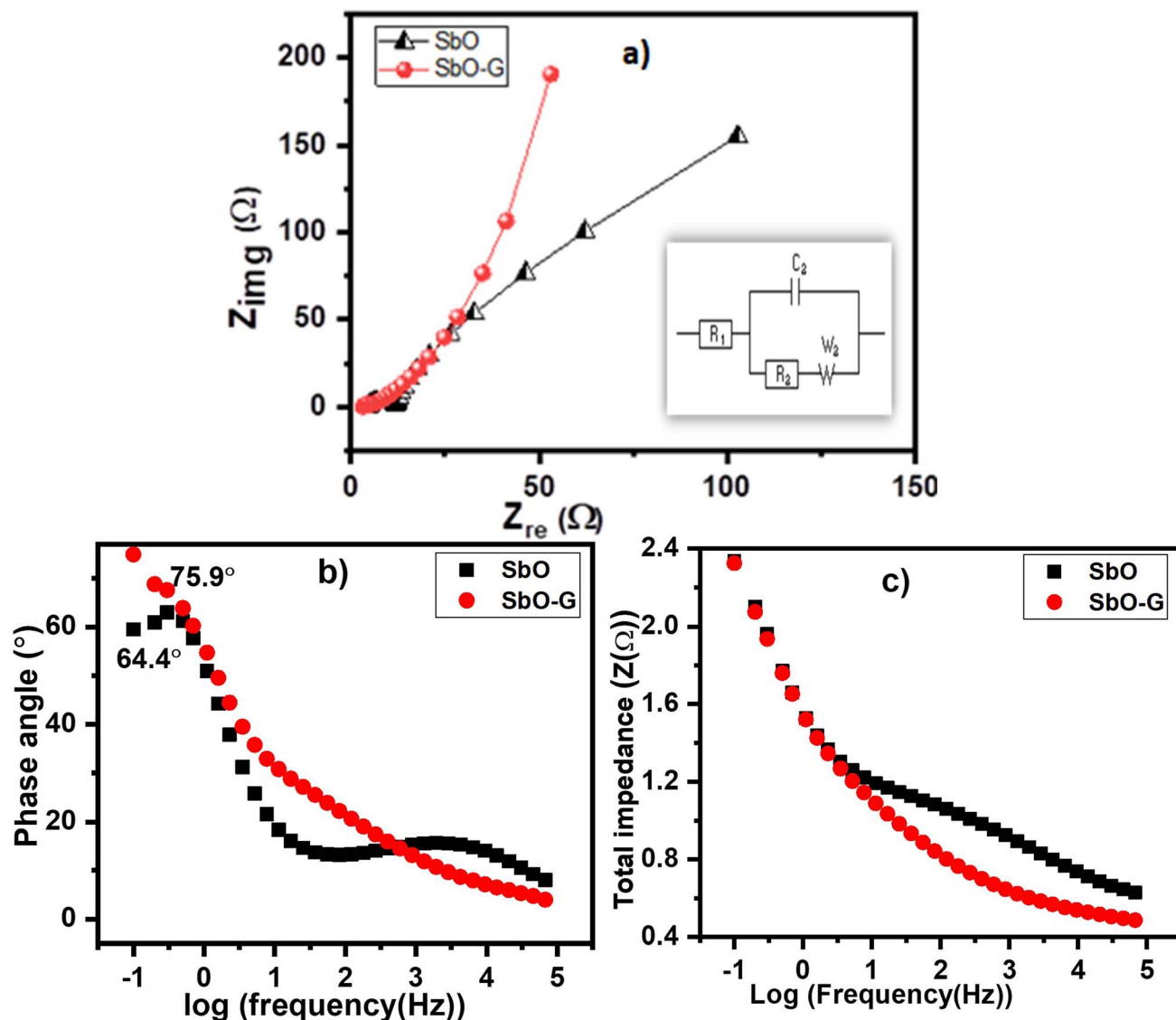
Fig. 6 (a) Nyquist plot of SbO and SbO-G, the inset is the equivalent circuit, (b) Bode plots of SbO and SbO-G, (c) total impedance plots of SbO and SbO-G.

specific capacitance at increased current density could be attributed to the limited flow of electrolyte ions into the active material's inner sites.[42]

3.3.3 Electrochemical impedance spectroscopy. As illustrated in Fig. 6a, Nyquist plots were used to analyze the electrochemical impedance spectroscopy (EIS) data and were displayed with an equivalent circuit inset.[43] In the high-frequency region, the intersection of the curve at the real component reveals the bulk resistance of the electrochemical system. This includes ionic resistance from the electrolytes, intrinsic grain to grain resistance of the electrode, and contact resistance at the interphase between the active material and the substrate.[44,45] The radius of the semicircle in the high-frequency region displays the charge-transfer process, at the interface of the electrode and the electrolyte. As we approach lower frequencies the semicircle breaks into a 45° nearly vertical line which is related to the Warburg (W_2) diffusion of ions within the

electrode inter-phase.[33] The EIS graphs demonstrated that SbO (4.8 Ω) had a greater R_s than SbO-G (3.2 Ω). SbO also shows a small semi-circle in the high-frequency region; however, with the addition of graphene the semi-circle disappears given a near-perfect capacitive response. SbO and SbO-G have fitting R_{ct} values of 7.35 and 3.75 Ω respectively. Also, as observed in the curve, the SbO-G electrodes exhibit better capacitive behaviour with an almost vertical line.[46] The slope of the 45° section of the curves in the intermediate frequency area was

Table 3 EIS curve fitting of SbO and SbO-G electrode materials

Sample	R_s (Ω)	CPE (μF)	R_{ct} (Ω)	W^2 (Ω s$^{-\frac{1}{2}}$)	Phase angle (°)
SbO	5.561	5.54	7.46	154.3	64.4
SbO-G	3.203	0.22	1.51	42.39	75.7

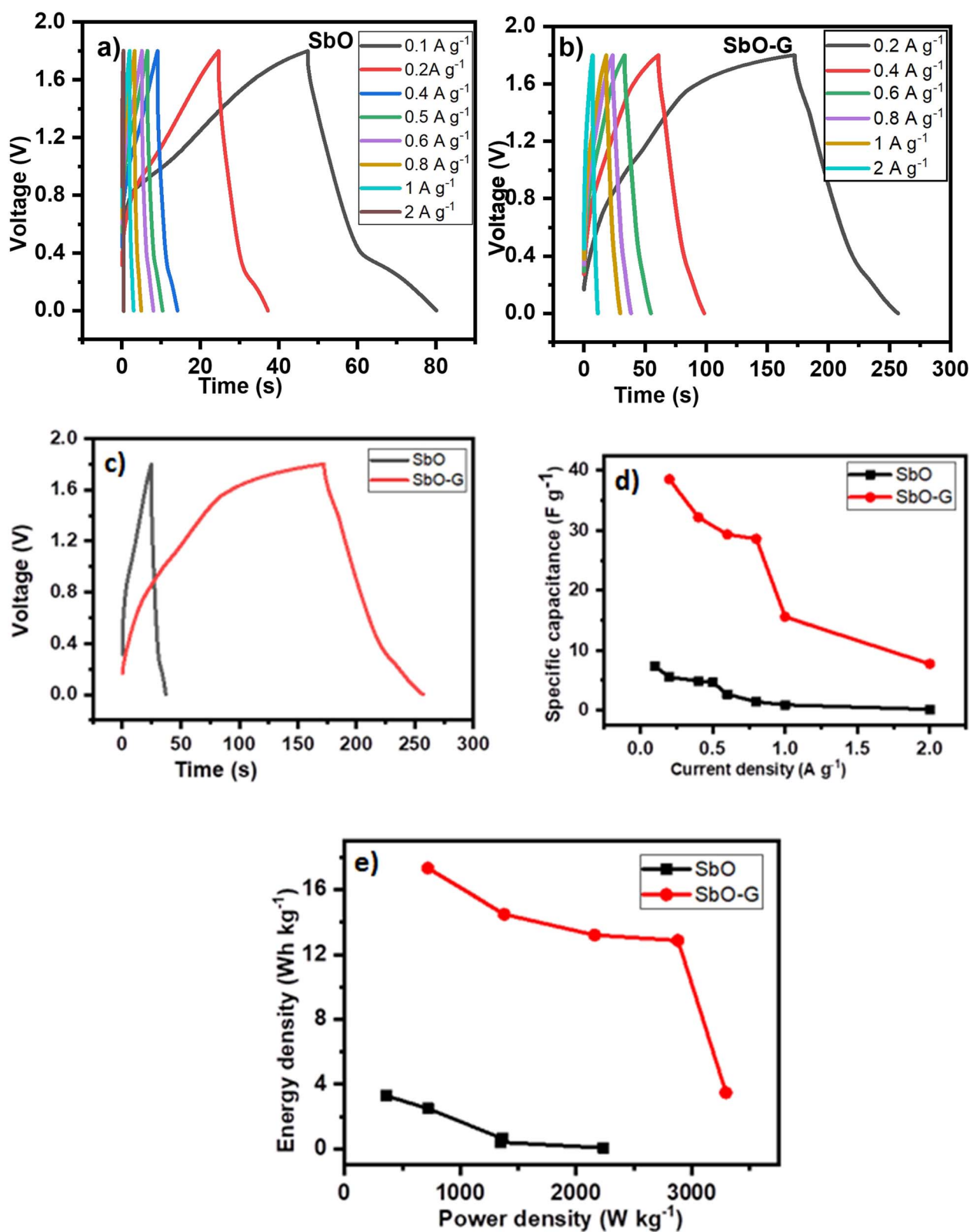© 2023 The Author(s). Published by the Royal Society of Chemistry

Fig. 7 AC//SbO and AC//SbO-G: (a and b) GCD plots at different current densities, (c) GCD plots comparing their charge and discharge profile at 0.2 A g^{-1} current density, (d) relationship between specific capacitance and current density (e) is the Ragone plot. All analysis was done in 1 M Li$_2$SO$_4$ electrolyte.

used to illustrate the Warburg resistance, which indicates ion diffusion/transport in the electrolyte and its relationship to frequencies. Furthermore, the Warburg resistance value (Table 3) is lower in SbO-G. Because of the low charge transfer resistance and lower diffusion effect, relatively reversible reactions can occur at the interface, which may explain the rectangular voltammogram of both materials and why the rectangular nature is retained even at high scan rates.

The Bode plot from the EIS data is shown as the phase angle and total impedance plot in Fig. 6b. The phase angle for SbO was 64.4° while that of SbO-G was 75.7°. The phase angle of SbO-G is closer to 90°, therefore, showing more capacitive phase angles as seen in the Warburg diffusion area. It is clear from the face angle that the materials store charges utilizing both the EDL and the pseudocapacitive mechanisms. The magnitude of total impedance was lowest in SbO-G as seen in Fig. 6c. The constant phase element (CPE) was also derived from the Bode total impedance plot. The CPE impedance is given by

$$Z_{CPE} = a^{-1}(jw)^{-n} \tag{3}$$

where a is the frequency-independent constant related to the roughness of the surface features, and the exponent n is determined by the slope of $\log z$ *vs.* $\log f$. The coefficient 'a' is resistive when $n = 0$, capacitive for $n = 1$ and a Warburg impedance (charge transfer impedance) for $n = 0.5$. The value of n for SbO and SbO-G was 0.78 and 0.69 respectively. The change in n confirms a change in the morphology of the material, both values show that the materials are capacitive as their values approach 1 (ref. 47). The total CPE values obtained from the fitted Nyquist plot are shown in Table 3.

3.4 Device fabrication

To investigate the potential of as-synthesized SbO and SbO-G nanoparticles in a full-cell configuration, an ASC with SbO/SbO-G as the positive electrode and activated carbon as the negative electrode material was designed. The charge storage in activated carbon occurs *via* the creation of an electrical double layer. The performance of AC in an aqueous solution of 1 M Li_2SO_4 in a half-cell arrangement with the SbO electrode was done. This ascertained the suitability of activated carbon as a negative electrode (Fig. 10 ESI†).

3.4.1 Galvanostatic charge discharge. The GCD plot as shown in Fig. 7a and b was obtained at different current densities (0.1 A g^{-1}, 0.2 A g^{-1}, 0.4 A g^{-1}, 0.5 A g^{-1}, 0.6 A g^{-1}, 0.8 A g^{-1}, 1 A g^{-1} and 2 A g^{-1}). The capacitance at each current density was calculated and the result is as shown in Tables 4 and 5. The result showed an improved performance in the SbO-G device compared to the SbO electrode device. Fig. 7d shows the relationship between the capacitance and the current density, the capacitance reduced with an increase in the current density. At a current density of 0.2 A g^{-1}, SbO-G has a specific capacitance of 32.89 F g^{-1}, which is higher than that of SbO (5.5 F g^{-1}). Notably, as the current density increased to 1 A g^{-1}, SbO-G maintained a high capacitance of 9.33 F g^{-1}, retaining 64% of its capacitance. The SbO device, on the other hand, exhibits poorer capacitance retention of 12.6%, indicating that the

Table 4 Capacitance, ED and PD of the activated carbon//SbO carbon device from the GCD data

Current density (A g^{-1})	Capacitance (F g^{-1})	PD (W kg^{-1})	ED (W h kg^{-1})
0.1	7.30	360.00	3.29
0.2	5.55	720.00	2.50
0.4	4.89	1440.00	2.20
0.5	4.66	1800.00	2.10
0.6	2.68	1388.57	1.21
0.8	1.43	1364.21	0.64
1	0.92	1350.00	0.41
2	0.15	2234.48	0.07

Table 5 Capacitance, ED and PD of activated carbon//SbO-G carbon device from the GCD data

Current density (A g^{-1})	Capacitance (F g^{-1})	PD (W kg^{-1})	ED (W h kg^{-1})
0.2	32.89	360.00	14.80
0.4	29.33	720.00	13.20
0.5	25.42	1440.00	11.44
0.6	24.82	1800.00	11.17
0.8	24.15	2160.00	10.87
1	21.16	2880.00	9.52
2	19.33	3600.00	8.70

structure of the graphene improved electrolyte ion diffusion. The specific energy and power were calculated according to the following equations:

$$E_{sp}(\text{W h kg}^{-1}) = \frac{CV^2}{2m} \times \frac{1}{3.6} \tag{4}$$

$$P_{max}(\text{W kg}^{-1}) = \frac{E}{\Delta t} \times 3600 \tag{5}$$

where C (F g^{-1}) is the specific capacitance determined from eqn (2), V is the maximum working potential, m (kg) is the mass of the active material in the electrode, and Δt is the capacitor's discharge time. Fig. 7e is a Ragone plot which depicts the relationship between the asymmetric device's energy density and power density, at various current densities. An ideal supercapacitor device would have a high energy density while also having a high-power density. Interestingly, the asymmetric C_s cell had the highest energy density of 2.50 W h kg^{-1}, at a power density of 720 W kg^{-1}, at 0.2 A g^{-1} current density for SbO, while SbO-G delivered an energy density of 14.8 W h kg^{-1}, at a power density of 360 W kg^{-1}, at 0.2 A g^{-1} current density. The energy density and power density were enhanced by the addition of graphene which led to increased surface area for charge–discharge.

3.4.2 Electrochemical impedance spectroscopy. Fig. 8a is the Nyquist plot of the SbO and SbO-G asymmetric devices. The inset is the fitted equivalent circuit data and the parameters obtained are represented in Table 6 below. The EIS is lower in the SbO-G (1.33 Ω) than in the SbO material (1.5 Ω). Also, the

impedance of the charge-transfer process at the interface of the electrode and the electrolyte was much lower for SbO-G (0.7 Ω) as compared to SbO (13.7 Ω), as can be seen by the smaller semicircle in the high-frequency area. This shows that more facile charge transfer occurred between the Li$^+$ and SO$_4^{2-}$ ions and SbO-G.[48,49] A well-defined, near-vertical, and shorter Warburg area part in the SbO-G device compared to the SbO device demonstrates that the ions in the electrolyte have a short and equal diffusion path length. Thus, because of the low charge transfer resistance and lower diffusion effect, relatively reversible reactions can occur at the interface, which explains the shape of the voltammogram and GCD profile.[46] The Bode plot from the EIS data is shown as the phase angle and total impedance plot in Fig. 8b. The phase angle of SbO is 68.06° while that of SbO-G device is 72.5°, indicating a capacitive behaviour which is from the contribution of both EDLC and pseudocapacitance. The magnitude of total impedance (Fig. 8c) had a value of 0.25 Ω for SbO and 0.12 Ω for SbO-G. Both Bode plots confirm a capacitive electrode.

Table 6 EIS curve fitting data of AC//SbO and AC//SbO-G electrode material

Electrolytes	R_s (Ω)	CPE (μF)	R_{ct} (Ω)	W^2 (Ω s$^{-\frac{1}{2}}$)	Phase angle (°)
SbO	1.5	1.74	13.7	17.79	68.06
SbO-G	1.33	14.72	0.7	15.42	72.5

3.4.3 Cycle life. Long cycle life is an important criterion for supercapacitors, the cycling stability was studied using the galvanostatic charge–discharge techniques at a current density of 0.5 A g^{-1} and a voltage range of 0–1.8 V. Fig. 9a shows that the SbO device remained stable for more than 3500 charging and discharging cycles, and retained ∼58% of its initial capacitance. However, the system maintained a 100% Coulombic efficiency throughout the period. As seen in the inset, the shape of the CV plot changed after the cycling. This is due to material distortion caused by the volume expansion of the Sb metal as a result of
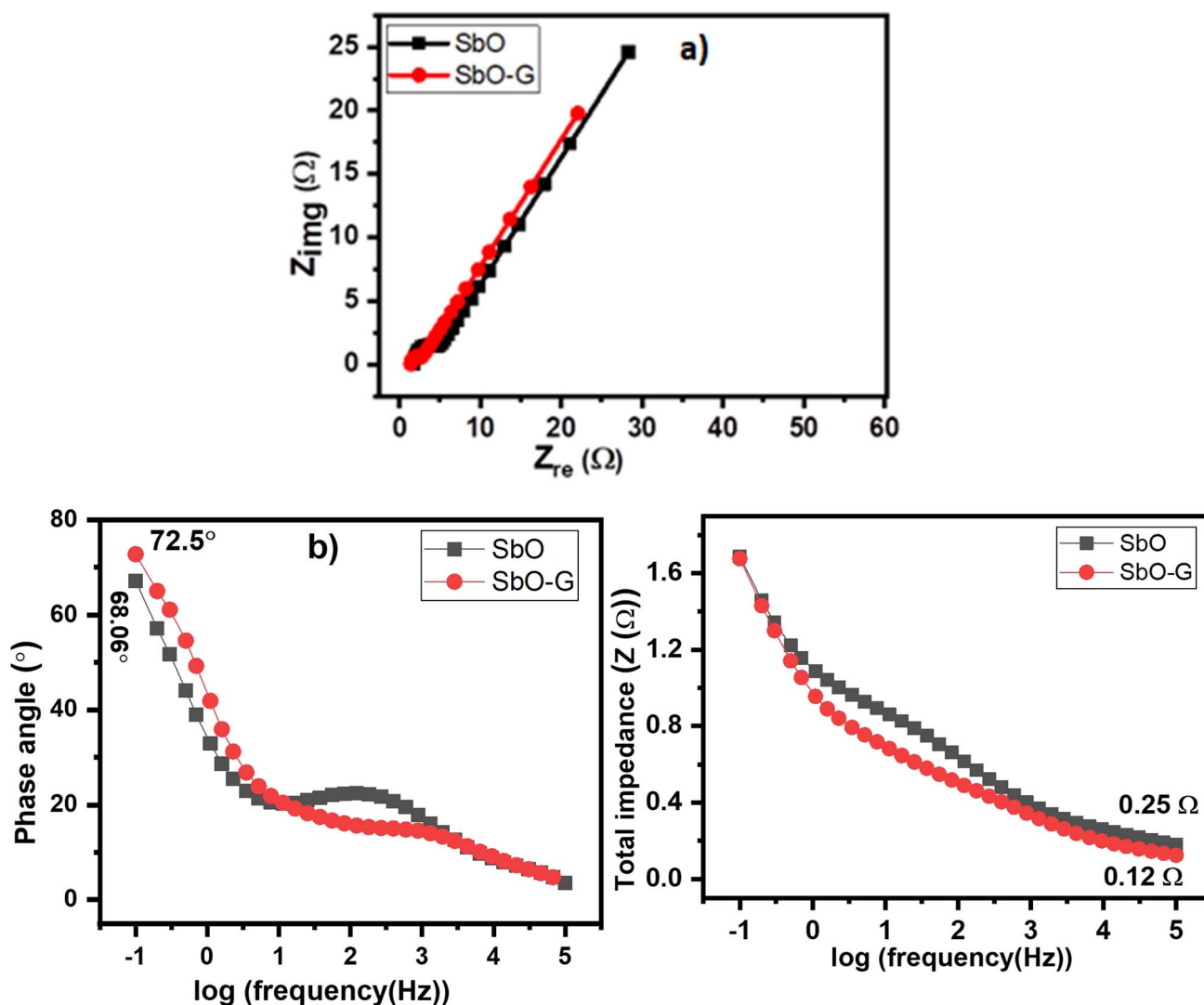

Fig. 8 EIS results represented as (a) the Nyquist plot (the inset is the equivalent circuit), (b) Bode plots, (c) total impedance plots.
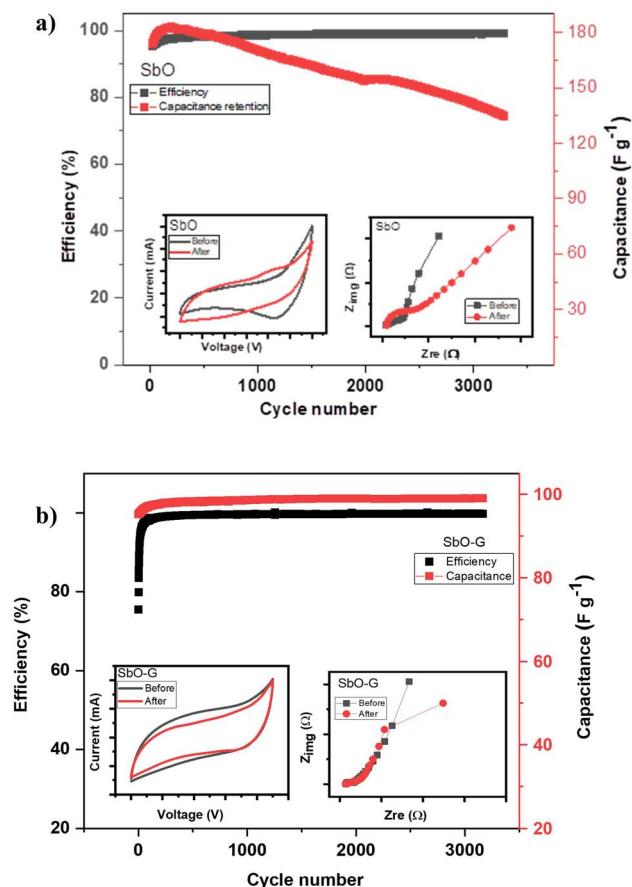
Fig. 9 Cycling stability of (a) AC//SbO and (b) AC//SbO-G super-capacitor over 4500 cycles in 1 M Li$_2$SO$_4$. The inset in (a and b) is the CV plot (50 mV s^{-1}) and EIS plot before and after cycling.

ion migration in and out of its pores.[48,50] The EIS of the device also changed after the cycling. The SbO-G device showed better capacitance retention as seen in Fig. 9b. The device maintained 100% capacitance retention after the cycling test. This is evident in the voltammogram which did not change after the charge and discharge test. The Coulombic efficiency was also maintained at 100% throughout the cycling. This improved stability is because of the incorporation of a more stable carbon matrix, thus improving the cycle life of the device. The EIS plot changed in the Warburg area, showing a more diffusion-controlled reaction.[2]

4. Conclusion

SbO and SbO-G were synthesized as electrodes for super-capacitors using the microwave assisted method. For the SbO-G samples, SbO nanoparticles are well distributed on the graphene sheets with a size of 10–50 nm acting as spacers between the graphene sheets. The charge storage mechanism visible in the CV curve of SbO is nearly rectangular and identical to the EDLC charge storage mechanism. The total capacitance increased from 25.11 F g^{-1} for the SbO to 98.00 F g^{-1} for the SbO-G. The increased specific capacitance of SbO-G demonstrates a positive synergistic effect of graphene nanosheets and

SbO. This is due to the utilization of the combined advantages of separated graphene nanosheets, and a high conductive network of fine SbO nanoparticles. SbO and SbO-G were used to fabricate an asymmetric supercapacitor device as a positive electrode, while activated carbon was used as the negative electrode. The asymmetric C_s cell delivered a maximum energy density of 2.52 W h kg^{-1}, at a power density of 720 W kg^{-1}, at 0.2 A g^{-1} current density for SbO, while SbO-G delivered an energy density of 14.80 W h kg^{-1}, at a power density of 360 W kg^{-1}, at the same current density. The energy density and power density were enhanced by the addition of graphene which led to increased surface area for charge discharge. This result shows that, apart from the conventional ruthenium oxide and carbon material used for supercapacitors, antimony oxides upon opti-mization will result in an excellent electrode material for energy storage. This study opens a new horizon for the exploration of new categories of nanomaterials, like 'antimony oxide-based materials' for supercapacitor application.

Author contributions

Emmanuel Iwuoha conceived and conceptualized the idea, he also supervised the findings of the project. Chinwe Ikpo and Miranda Ndipingwi verified the experimental and analytical methods and supervised the findings of this work. Christoper Nolly contributed to sample preparations. Precious Ekwere developed the theoretical formalism, carried out the experi-ment, manufactured the samples and characterized, processed the experimental data, drafted the manuscript and designed the figures, performed the calculations, and aided in interpreting the results. All authors provided critical feedback and helped shape the research, analysis and manuscript.

Conflicts of interest

There are no conflicts to declare.

Acknowledgements

References

1 Y. Anil Kumar, K. Dasha Kumar and H. J. Kim, A novel electrode for supercapacitors: Efficient PVP-assisted synthesis of Ni$_3$S$_2$ nanostructures grown on Ni foam for energy storage, *Dalton Trans.*, 2020, **49**, 4050–4059, DOI: **10.1039/d0dt00191k**.

2 A. Noori, M. F. El-kady, M. S. Rahmanifar, R. B. Kaner and M. F. Mousavi, Chem Soc Rev metrics for batteries, supercapacitors and beyond, *Chem. Soc. Rev.*, 2019, **48**, 1272–1341, DOI: **10.1039/c8cs00581h**.

3 N. Matinise, N. Mayedwa, X. G. Fuku, N. Mongwaketsi and M. Maaza, Green synthesis of cobalt (II, III) oxide nanoparticles using Moringa Oleifera natural extract as high electrochemical electrode for supercapacitors, *AIP Conf. Proc.*, 2018, **1962**, 1, DOI: 10.1063/1.5035543.

4 T. E. Mabokela, A. C. Nwanya, M. M. Ndipingwi, S. Kaba, P. Ekwere, S. T. Werry, C. O. Ikpo, K. D. Modibane and E. I. Iwuoha, Review—Recent Advances on High-Capacity Li Ion-Rich Layered Manganese Oxide Cathodes, *J. Electrochem. Soc.*, 2021, **168**, 070530, DOI: 10.1149/1945-7111/AC0B58.

5 M. Filella, N. Belzile and Y. W. Chen, Antimony in the environment: A review focused on natural waters I. Occurrence, *Earth-Sci. Rev.*, 2002, **57**, 125–176, DOI: 10.1016/S0012-8252(01)00070-8.

6 Y. Yuan, S. Jan, Z. Wang and X. Jin, A simple synthesis of nanoporous Sb/C with high Sb content and dispersity as an advanced anode for sodium ion batteries, *J. Mater. Chem. A*, 2018, **6**, 5555–5559, DOI: 10.1039/c8ta00592c.

7 Y. B. Kamenev, A. V Kiselevich, E. I. Ostapenko and Y. V Skachkov, Antimony-free alloys for unattended (sealed) lead batteries, *Russ. J. Appl. Chem.*, 2002, **75**, 548–551, DOI: 10.1023/A:1019548510196.

8 M. Kosai, S. Yasukawa, S. Osumi and M. Tsubota, Effect of antimony on premature capacity loss of lead/acid batteries, *J. Power Sources*, 1997, **67**, 43–48, DOI: 10.1016/S0378-7753(97)02496-8.

9 M. Ciszewski, A. Mianowski, G. Nawrat and P. Szatkowski, Reduced Graphene Oxide Supported Antimony Species for High-Performance Supercapacitor Electrodes, *ISRN Electrochem.*, 2014, **2014**, 1–7, DOI: 10.1155/2014/826832.

10 R. K. Sahoo, S. Singh, J. M. Yun, S. H. Kwon and K. H. Kim, Sb_2S_3 Nanoparticles Anchored or Encapsulated by the Sulfur-Doped Carbon Sheet for High-Performance Supercapacitors, *ACS Appl. Mater. Interfaces*, 2019, **11**, 33966–33977, DOI: 10.1021/acsami.9b11028.

11 B. Xiao, G. Wu, T. Wang, Z. Wei, Y. Sui, B. Shen, J. Qi, F. Wei, Q. Meng, Y. Ren, X. Xue, J. Zheng, J. Mao, K. Dai and Q. Yan, Tin antimony oxide @ graphene as a novel anode material for lithium ion batteries, *Ceram. Int.*, 2021, **48**(2), 2118–2123, DOI: 10.1016/j.ceramint.2021.09.300.

12 T. Le Hai, L. C. Hung, T. T. B. Phuong, B. T. T. Ha, B. S. Nguyen, T. D. Hai and V. H. Nguyen, Multiwall carbon nanotube modified by antimony oxide (Sb_2O_3/MWCNTs) paste electrode for the simultaneous electrochemical detection of cadmium and lead ions, *Microchem. J.*, 2020, **153**, 104456, DOI: 10.1016/j.microc.2019.104456.

13 O. M. Lopez, M. C. Hegy and T. M. Missimer, Statistical comparisons of grain size characteristics, hydraulic conductivity, and porosity of barchan desert dunes to coastal dunes, *Aeolian Res.*, 2020, **43**, 100576, DOI: 10.1016/j.aeolia.2020.100576.

14 T. E. Mabokela, A. C. Nwanya, M. M. Ndipingwi, S. T. Yussuf, P. I. Ekwere, O. V. Uhuo, C. O. Ikpo, K. D. Modibane and E. I. Iwuoha, Nanostructured europium-doped layered lithium manganese oxide as a prospective cathode material for aqueous lithium-ion battery, *Electrochim. Acta*, 2023, **441**, 141865, DOI: 10.1016/J.ELECTACTA.2023.141865.

15 M. H. Chakrabarti, E. P. L. Roberts, C. Bae and M. Saleem, Ruthenium based redox flow battery for solar energy storage, *Energy Convers. Manage.*, 2011, **52**, 2501–2508, DOI: 10.1016/j.enconman.2011.01.012.

16 X. Fuku, N. Matinise, M. Masikini, K. Kasinathan and M. Maaza, An electrochemically active green synthesized polycrystalline NiO/MgO catalyst: Use in photo-catalytic applications, *Mater. Res. Bull.*, 2018, **97**, 457–465, DOI: 10.1016/j.materresbull.2017.09.022.

17 I. S. El-Hallag, M. N. El-Nahass, S. M. Youssry, R. Kumar, M. M. Abdel-Galeil and A. Matsuda, Facile in-situ simultaneous electrochemical reduction and deposition of reduced graphene oxide embedded palladium nanoparticles as high performance electrode materials for supercapacitor with excellent rate capability, *Electrochim. Acta*, 2019, **314**, 124–134, DOI: 10.1016/j.electacta.2019.05.065.

18 P. Ekwere, M. Ndipingwi, C. Ikpo, S. Yussuf, K. Nwambaekwe, O. Uhuo and E. Iwuoha, High stability asymmetric supercapacitor cell developed with novel microwave-synthesized graphene-stabilized ruthenium antimonide nanomaterial, *J. Energy Storage*, 2023, **63**, 106853, DOI: 10.1016/j.est.2023.106853.

19 W. Xu, H. Wang, R. Liu, X. Zhao and J. Qu, The mechanism of antimony(III) removal and its reactions on the surfaces of Fe–Mn Binary Oxide, *J. Colloid Interface Sci.*, 2011, **363**, 320–326, DOI: 10.1016/J.JCIS.2011.07.026.

20 A. L. J. Pereira, L. Gracia, D. Santamaría-Pérez, R. Vilaplana, F. J. Manjón, D. Errandonea, M. Nalin and A. Beltrán, Structural and vibrational study of cubic Sb_2O_3 under high pressure, *Phys. Rev. B: Condens. Matter Mater. Phys.*, 2012, **85**, 174108, DOI: 10.1103/PhysRevB.85.174108.

21 M. Assebban, C. Gibaja, M. Fickert, I. Torres, E. Weinreich, S. Wolff, R. Gillen, J. Maultzsch, M. Varela, S. Tan Jun Rong, K. P. Loh, E. G. Michel, F. Zamora and G. Abellán, Unveiling the oxidation behavior of liquid-phase exfoliated antimony nanosheets, *2D Mater*, 2020, **7**, 025–039, DOI: 10.1088/2053-1583/ab755e.

22 N. E. Drewett, I. M. Aldous, J. Zou and L. J. Hardwick, In situ Raman spectroscopic analysis of the lithiation and sodiation of antimony microparticles, *Electrochim. Acta*, 2017, **247**, 296–305, DOI: 10.1016/j.electacta.2017.07.030.

23 K. Yang, T. Zhang, B. Wei, Y. Bai, S. Jia, G. Cao, R. Jiang, C. Zhang, E. Gao, X. Chang, J. Li, S. Li, D. Zhu, R. Tai, H. Zhou, J. Wang, M. Zeng, Z. Wang and L. Fu, Ultrathin high-κ antimony oxide single crystals, *Nat. Commun.*, 2020, **11**, 7–12, DOI: 10.1038/s41467-020-16364-9.

24 H. Zhang, K. Sun, Z. Feng, P. Ying and C. Li, Studies on the SbO_x species of SbO_x/SiO_2 catalysts for methane-selective oxidation to formaldehyde, *Appl. Catal., A*, 2006, **305**, 110–119, DOI: 10.1016/j.apcata.2006.02.038.

25 Q. Zhang, Z. Hu, Y. Yang, Z. Zhang, X. Wang, X. Yang, Y. An and B. Guo, Metal organic frameworks-derived porous carbons/ruthenium oxide composite and its application in

supercapacitor, *J. Alloys Compd.*, 2018, **735**, 1673–1681, DOI: **10.1016/j.jallcom.2017.11.268**.

26 A. Simion, N. Candu, B. Cojocaru, S. Coman, C. Bucur, A. Forneli, A. Primo, I. C. Man, V. I. Parvulescu and H. Garcia, Nanometer-thick films of antimony oxide nanoparticles grafted on defective graphenes as heterogeneous base catalysts for coupling reactions, *J. Catal.*, 2020, **390**, 135–149, DOI: **10.1016/j.jcat.2020.07.033**.

27 T. K. Das, S. Banerjee, M. Pandey, B. Vishwanadh, R. J. Kshirsagar and V. Sudarsan, Effect of surface functional groups on hydrogen adsorption properties of Pd dispersed reduced graphene oxide, *Int. J. Hydrogen Energy*, 2017, **42**, 8032–8041, DOI: **10.1016/j.ijhydene.2016.12.024**.

28 S. Wolff, S. Roscher, F. Timmermann, M. V Daniel, F. Speck, M. Wanke, M. Albrecht and T. Seyller, Quasi-Freestanding Graphene on SiC(0001) by Ar-Mediated Intercalation of Antimony: A Route Toward Intercalation of High-Vapor-Pressure Elements, *Ann. Phys.*, 2019, **531**, 1900199, DOI: **10.1002/andp.201900199**.

29 I. Martini, E. Chevallay, V. Fedosseev, C. Hessler, H. Neupert, V. Nistor, and M. Taborelli, Surface characterization at CERN of photocathodes for photoinjector applications, in *6th Int. Part. Accel. Conf. IPAC 2015*, 2015, pp. 1703–1705, **http://xpssimplified.com/periodictable.ph**, accessed November 11, 2021.

30 Y. Lin, Z. Tian, L. Zhang, J. Ma, Z. Jiang, B. J. Deibert, R. Ge and L. Chen, Chromium-ruthenium oxide solid solution electrocatalyst for highly efficient oxygen evolution reaction in acidic media, *Nat. Commun.*, 2019, **10**, 1–13, DOI: **10.1038/s41467-018-08144-3**.

31 H. Xue, K. Chen, Q. Zhou, D. Pan, Y. Zhang and Y. Shen, Antimony selenide/graphene oxide composite for sensitive photoelectrochemical detection of DNA methyltransferase activity, *J. Mater. Chem. B*, 2019, **7**, 6789–6795, DOI: **10.1039/c9tb01541h**.

32 P. Molaei and I. Kazeminezhad, Extended photocurrent performance of antimony trisulfide/reduced graphene oxide composite prepared via a facile hot-injection route, *Ceram. Int.*, 2018, **44**, 13191–13196, DOI: **10.1016/j.ceramint.2018.04.144**.

33 Y. Gong, D. Li, Q. Fu and C. Pan, Influence of graphene microstructures on electrochemical performance for supercapacitors, *Prog. Nat. Sci.: Mater. Int.*, 2015, **25**, 379–385, DOI: **10.1016/j.pnsc.2015.10.004**.

34 K. Sharma, A. Arora and S. K. Tripathi, Review of supercapacitors: Materials and devices, *J. Energy Storage*, 2019, **21**, 801–825, DOI: **10.1016/j.est.2019.01.010**.

35 S. Ardizzone and G. Fregonara, Inner" and "outer" active surface of RuO2 electrodes, *Electrochim. Acta*, 1990, **35**(1), 263–267.

36 D. Galizzioli, F. Tantardini and S. Trasatti, Ruthenium dioxide: a new electrode material. I. Behaviour in acid solutions of inert electrolytes, *J. Appl. Electrochem.*, 1974, **4**, 57–67, DOI: **10.1007/BF00615906**.

37 Q. Xue, H. Gan, Y. Huang, M. Zhu, Z. Pei, H. Li, S. Deng, F. Liu and C. Zhi, Boron Element Nanowires Electrode for Supercapacitors, *Adv. Energy Mater.*, 2018, **8**, 1–8, DOI: **10.1002/aenm.201703117**.

38 B. J. Choudhury, K. Roy and V. S. Moholkar, Improvement of Supercapacitor Performance through Enhanced Interfacial Interactions Induced by Sonication, *Ind. Eng. Chem. Res.*, 2021, **60**, 7611–7623, DOI: **10.1021/acs.iecr.1c00279**.

39 T. Pettong, P. Iamprasertkun, A. Krittayavathananon, P. Sukha, P. Sirisinudomkit, A. Seubsai, M. Chareonpanich, P. Kongkachuichay, J. Limtrakul and M. Sawangphruk, High-Performance Asymmetric Supercapacitors of MnCo2O4 Nanofibers and N-Doped Reduced Graphene Oxide Aerogel, *ACS Appl. Mater. Interfaces*, 2016, **8**, 34045–34053, DOI: **10.1021/acsami.6b09440**.

40 J. Yan, T. Wei, W. Qiao, B. Shao, Q. Zhao, L. Zhang and Z. Fan, Rapid microwave-assisted synthesis of graphene nanosheet/Co_3O_4 composite for supercapacitors, *Electrochim. Acta*, 2010, **55**, 6973–6978, DOI: **10.1016/j.electacta.2010.06.081**.

41 C. Wang, J. Zhao, S. Luo and X. Yu, Improved Pseudocapacitive Performance of Graphene Architectures Modulating by Nitrogen/Phosphorus Dual-Doping and Steam-Activation, *Macromol. Res.*, 2021, **29**, 582–588, DOI: **10.1007/s13233-021-9075-7**.

42 M. Dvoyashkin, D. Leistenschneider, J. D. Evans, M. Sander and L. Borchardt, Revealing the Impact of Hierarchical Pore Organization in Supercapacitor Electrodes by Coupling Ionic Dynamics at Micro- and Macroscales, *Adv. Energy Mater.*, 2021, **11**, 2100700, DOI: **10.1002/aenm.202100700**.

43 D. Qu, Studies of the activated mesocarbon microbeads used in double-layer supercapacitors, *J. Power Sources*, 2002, **109**, 403–411.

44 D. Mandal, P. Routh, A. K. Mahato and A. K. Nandi, Electrochemically modified graphite paper as an advanced electrode substrate for supercapacitor application, *J. Mater. Chem. A*, 2019, **7**, 17547–17560, DOI: **10.1039/c9ta04496e**.

45 C. Nolly, C. O. Ikpo, M. M. Ndipingwi, P. Ekwere and E. I. Iwuoha, Pseudocapacitive Effects of Multi-Walled Carbon Nanotubes-Functionalised Spinel Copper Manganese Oxide, *Nanomaterials*, 2022, **12**, 3514, DOI: **10.3390/nano12193514**.

46 N. Bundaleska, J. Henriques, M. Abrashev, A. M. Botelho do Rego, A. M. Ferraria, A. Almeida, F. M. Dias, E. Valcheva, B. Arnaudov, K. K. Upadhyay, M. F. Montemor and E. Tatarova, Large-scale synthesis of free-standing N-doped graphene using microwave plasma, *Sci. Rep.*, 2018, **8**, 1–11, DOI: **10.1038/s41598-018-30870-3**.

47 H. Wei, C. He, J. Liu, H. Gu, Y. Wang, X. Yan, J. Guo, D. Ding, N. Z. Shen, X. Wang, S. Wei and Z. Guo, Electropolymerized polypyrrole nanocomposites with cobalt oxide coated on carbon paper for electrochemical energy storage, *Polymer (Guildf)*, 2015, **67**, 192–199, DOI: **10.1016/J.POLYMER.2015.04.064**.

48 D. Mandal, P. Routh, A. K. Mahato and A. K. Nandi, Electrochemically modified graphite paper as an advanced electrode substrate for supercapacitor application, *J. Mater. Chem. A*, 2019, **7**, 17547–17560, DOI: **10.1039/c9ta04496e**.

49 K. Yang, K. Cho and S. Kim, Effect of carbon black addition on thermal stability and capacitive performances of supercapacitors, *Sci. Rep.*, 2018, **8**, 1–7, DOI: **10.1038/s41598-018-30507-5**.

50 S. Manoharan, D. Kesavan, P. Pazhamalai, K. Krishnamoorthy and S. J. Kim, Ultrasound irradiation mediated preparation of antimony sulfoiodide (SbSI) nanorods as a high-capacity electrode for electrochemical supercapacitors, *Mater. Chem. Front.*, 2021, **5**, 2303–2312, DOI: **10.1039/d0qm00863j**.